

# Possible instrumental effects on moments computation of the solar wind proton velocity distribution function: Helios observations

R. De Marco<sup>1</sup>, R. Bruno<sup>1</sup>, R. D'Amicis<sup>1</sup>, D. Telloni<sup>2</sup>, and D. Perrone<sup>3</sup>

<sup>1</sup> National Institute for Astrophysics, Institute for Space Astrophysics and Planetology, Via del Fosso del Cavaliere 100, 00133 Rome, Italy

e-mail: [rossana.demarco@inaf.it](mailto:rossana.demarco@inaf.it)

<sup>2</sup> National Institute for Astrophysics, Astrophysical Observatory of Turin, Via Osservatorio 20, 10025 Pino Torinese, Turin, Italy

<sup>3</sup> Italian Space Agency, Via del Politecnico snc, 00133 Rome, Italy

Received 27 November 2019 / Accepted 23 May 2020

## ABSTRACT

The solar wind is a highly turbulent medium in which most of the energy is carried by Alfvénic fluctuations. These fluctuations have a wide range of scales whose high-frequency tail can be relevant for the sampling techniques commonly used to detect the particle distribution in phase space in situ. We analyze the effect of Alfvénic fluctuations on moments computation of the solar wind proton velocity distribution for a plasma sensor, whose sampling time is comparable or even longer than the typical timescale of the velocity fluctuations induced by these perturbations. In particular, we numerically simulated the sampling procedure used on board Helios 2. We directly employed magnetic field data recorded by the Helios 2 magnetometer, when the s/c was immersed in fast wind during its primary mission to the Sun, to simulate Alfvénic fluctuations. More specifically, we used magnetic field data whose cadence of 4 Hz is considerably higher than that the plasma sensor needed to sample a full velocity distribution function, and we average these data to 1 Hz, which is the spin period of Helios. Density values, which are necessary to build Alfvénic fluctuations at these scales, are not available because the cadence of the Helios plasma data is 40.5 s. The adopted solution is based on the assumption that the available Helios plasma density power spectrum can be extended to the same frequencies as the magnetic field spectrum by extrapolating the power-law fit of the low-frequency range to the frequencies relevant for this study. Surrogate density values in the time domain are then obtained by inverse transforming this spectrum. We show that it cannot be excluded that relevant instrumental effects strongly contribute to generate interesting spectral and kinetic features that have been interpreted in the past literature as exclusively due to physical mechanisms.

**Key words.** turbulence – Sun: heliosphere – Sun: particle emission – instrumentation: detectors

## 1. Introduction

Turbulent fluctuations associated with interplanetary magnetic field and solar wind plasma parameters have been studied for decades since the first in situ measurements during the 1960s. These fluctuations, although highly disordered, prove to be rather self-similar, that is, fluctuations on different timescales show the same statistical features. In other words, if fluctuations of the same parameter at two different scales are normalized to their respective standard deviations, their probability distribution functions collapse onto each other. Self-similarity or scale invariance implies the existence of power laws governing the amplitude of the fluctuations at different scales (Kolmogorov 1941; Frisch 1995; Tu & Marsch 1995; Bruno & Carbone 2013). Coleman (1968), who first studied the spectral properties of magnetic field and velocity fluctuations as measured by Mariner 2 at about 1 AU, showed that the solar wind often exhibits a turbulent behavior over several frequency decades, within which the power density spectrum shows a robust power-law dependence. Later, during mid-1970s, solar wind observations by the Helios mission showed that this turbulent spectrum experiences a significant evolution during the wind expansion in the inner heliosphere (see related papers cited in the reviews by Tu & Marsch 1995; Bruno & Carbone 2013). However, the effects of the evolution were quite different for the fast and

slow wind. This behavior was due to the different nature of the fluctuations, that is, Alfvénic and uncompressive in the fast wind, non-Alfvénic and rather compressive in the slow wind (see Tu & Marsch 1995, Bruno & Carbone 2013 and related papers). Interestingly, another spectral feature that characterizes the different nature of turbulence in the fast and slow wind was the appearance of a remarkable flattening toward the high-frequency end of the spectrum of the proton number density fluctuations only within the fast wind (Marsch & Tu 1990). A less pronounced flattening was also present in the proton temperature (Tu et al. 1991) and in magnetic field intensity spectra (Bavassano et al. 1982). These spectral features, clearly present at short heliocentric distances, faded away with the distance from the Sun. Tu et al. (1989) noted that a similar spectral flattening and a similar radial evolution also belonged to the Alfvénic inward modes and suggested that the observed spectral features might be due to the parametric decay instability that, at short heliocentric distances, is experienced by large-amplitude forward Alfvén modes present within fast streams. The parametric decay instability (Goldstein 1978; Derby 1978; Sakai & Sonnerup 1983; Terasawa et al. 1986; Primavera et al. 1999, 2003; Bavassano et al. 2000; Malara et al. 2000, 2001; Bruno et al. 2004) is effective on large-amplitude circularly polarized Alfvén waves when the plasma  $\beta < 1$ . Through the instability process, the energy of the mother wave is redistributed

over three daughter waves, a forward-propagating Alfvén wave, with negligible amplitude, a backward-propagating Alfvén wave at lower frequency, and one compressive sound-like wave at higher frequency. Thus it looked reasonable to ascribe the observed high-frequency spectral flattening of both backward modes and number density fluctuations to this mechanism.

Another interesting feature is related to the intermittent character of the fluctuations. In this respect, Bruno et al. (2014) studied fast Alfvénic streams observed by Helios 2 in the inner heliosphere. They found that the intermittency of number density fluctuations, at odds with fluctuations of all the other solar wind parameters, decreases during the wind expansion. In contrast, within the slow and non-Alfvénic wind, density fluctuations do not show any clear radial evolution (Bruno et al. 2014). In particular, the same authors found that the intermittent events seem to derive from some non-Poissonian mechanism, and the behavior of density fluctuations generated in a numerical study of the nonlinear evolution of parametric instability was qualitatively similar to that observed in situ by Helios. Thus, the authors concluded that parametric decay might play a role in generating the observed spectral feature of the density fluctuations.

On the other hand, we cannot exclude a priori that instrumental effects might have altered the estimate of plasma parameters such as the proton number density. This suspicion derives from the consideration that Helios, as we describe in more detail in the following section, took a rather long time to sample the whole proton distribution function in phase space. The sampling time of the Helios plasma instrument was on the same order as the time period of Alfvénic fluctuations, which are particularly relevant within the fast wind at short heliocentric distances. These fluctuations could produce non-negligible oscillations of the particle velocity distribution function (VDF hereafter) in phase space during the sampling time (Perrone et al. 2014). Nicolaou et al. (2019) recently numerically evaluated the effects of turbulence velocity fluctuations on the expected measurements by the Proton Alpha Sensor (PAS) on board Solar Orbiter. The authors compared bulk parameters derived from statistical moments of their modeled turbulent environment to bulk parameters derived from simulated PAS measurements. Based on the short sampling time of about 1 s, they concluded that, in case of PAS measurements, the effects of turbulence would be minimum. In contrast, we show that the rather slow sampling time of the Helios plasma sensor had a non-negligible effect on the moments computation of the proton VDF. In particular, we show that interesting spectral and kinetic features observed in number density and proton temperature, which have been interpreted as exclusively due to physical mechanisms, might also hide relevant instrumental effects.

## 2. Numerical simulation

In this section we describe how we simulated the data sampling by means of an instrument with characteristics very similar to the quadrispherical analyzer E1/I1a for positive ions flown on board Helios (Schwenn et al. 1975). The simulated instrument has an energy per charge range between 155 keV/q to 15.32 keV/q divided into 32 channels that are logarithmically distributed, 9 elevation channels between  $-20^\circ$  and  $20^\circ$ , and 16 azimuths between  $-54.5^\circ$  and  $32.7^\circ$  sampled by mean of the spacecraft rotation. During each spin, which lasts 1 s, a matrix of  $16 \times 9$  counts for a given energy channel is acquired. The cadence of the plasma sampling is 40.5 s. However, only 32 s are necessary to step the entire energy range. The mock-up counts were simulated by taking into account that, for an electrostatic analyzer, the counts are related to the distribution function

according to the equation (see, e.g., Balogh 2005):

$$N = \int_T dt \int_v f(\mathbf{v}, t) A d\mathbf{v}, \quad (1)$$

where  $N$  is the number of particles acquired in the accumulation time  $T$ ,  $f(\mathbf{v}, t)$  is the distribution function, and  $A$  is a constant related to the sensitivity of the instrument. The distribution function was simulated by considering a bi-Maxwellian distribution whose density, velocity, and temperature change during the measurement process. More specifically, for each elementary measurement time  $i$ , we added to a constant bulk velocity a fluctuation given by  $\delta V_i = (\mathbf{B}_i - \langle \mathbf{B}_i \rangle) / \sqrt{4\pi\rho_i}$ , where  $\mathbf{B}_i$  is the magnetic field vector measured by the E2 instrument (Musmann et al. 1977),  $\langle \mathbf{B}_i \rangle$  is the average magnetic field in the entire selected period, and  $\rho_i$  is the mass density in the time interval  $i$ . We considered variations in the magnetic field with a cadence of 1 Hz, corresponding to the spin period of the satellite, and obtained downsampling data at 4 Hz resolution<sup>1</sup>. Because no plasma parameters are available at this frequency (the cadence is 40.5 s), we calculated the fluctuations assuming that the low-frequency part of the available spectra of density and temperature from Helios can be extrapolated to 1 Hz. The time series was then obtained by anti-transforming the spectrum as described below. In this way, during each spin period – corresponding to a single energy step – the sensor samples a distribution function that moves in the field of view according to the perturbation induced by the Alfvén wave. The left panel of Fig. 1 shows, from top to bottom, the bulk speed  $V_{sw}$ , the number density  $N$ , the proton temperature  $T_p$ , and the magnetic field intensity  $B$  at 40.5 s temporal resolution<sup>2</sup>. The data refer to a high-speed stream observed by Helios 2 at 0.3 AU during its first perihelion passage in 1976. This particular fast stream is well known in the literature for being rather uncompressive and highly Alfvénic (Bruno & Carbone 2013), as can be inferred from the rather constant value of the field intensity  $B$  and the proton number density  $N$  and from the remarkable fluctuations of the wind velocity and magnetic field components. The shaded area indicates the time interval from which we took the values for the number density  $N$  and proton temperature  $T_p$  to build the corresponding spectra that are shown in the middle and right panels of Fig. 1, respectively. These two spectra are characterized by a steep spectral scaling at low frequencies and a remarkable flattening at frequencies above  $\sim 10^{-4}$  Hz, which is quite more evident in  $N$ . As anticipated above, we need to infer values of the number density and proton temperature at 1 s scale in order to build Alfvénic fluctuations and to feed the simulation machinery with 1 s proton density and temperature values to simulate the appropriate distribution function. One way to create these data is to assume that the observed flattening is completely due to instrumental effects. In this hypothesis, we fit the low-frequency part of each spectrum and created an artificial spectrum, with the same constant scaling extending up to the highest frequency, which in our case corresponds to the Nyquist frequency of 1/2 Hz. To obtain the corresponding time series that was used as input in our simulation, we inversely transformed these spectra. As discussed in Stansby et al. (2018) and D’Amicis et al. (2019), the Helios proton temperature available at CDAWeb is a projection along the radial direction obtained from 1D distribution functions. However, we need to pass the temperature components as input of

<sup>1</sup> The magnetic field data at 4 Hz are available on the website <http://helios-data.ssl.berkeley.edu>

<sup>2</sup> Data are available on the website <https://cdaweb.sci.gsfc.nasa.gov>

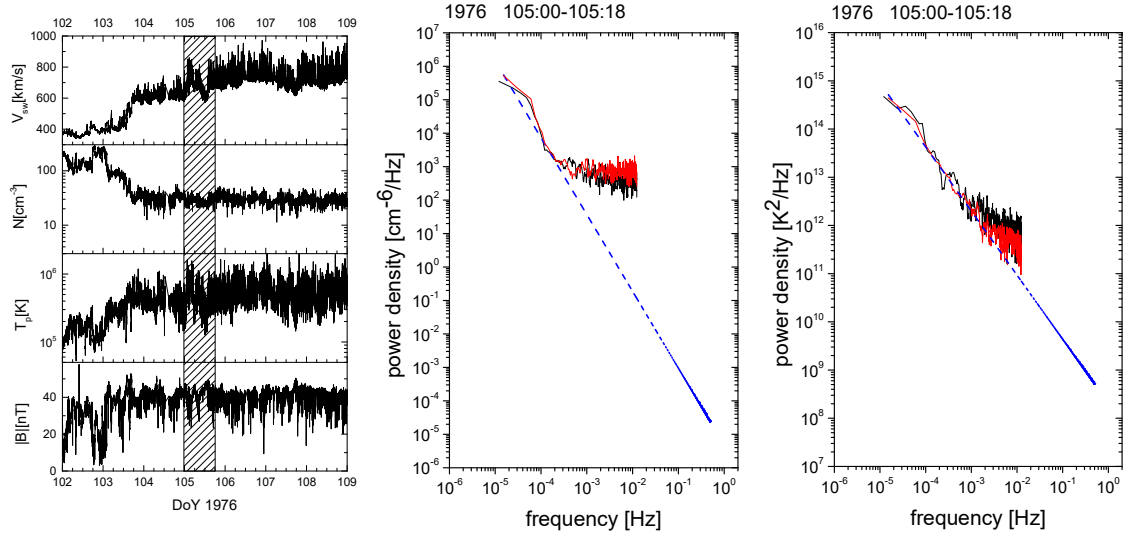


**Fig. 1.** *Left panel:* time series of the bulk speed  $V_{sw}$ , the number density  $N$ , the temperature  $T_p$ , and the magnetic field intensity  $B$  from part of the trailing edge of the fast wind stream encountered at 0.3 AU. The time interval we selected corresponds to the shaded area. *Middle panel:* power spectral densities of the number density for real data (black line) and simulated data (red line) for the selected time interval. The dashed blue line refers to the fit of the low-frequency part of the spectrum. *Right panel:* power spectral densities of the radial temperature for real data (black line) and simulated data (red line) for the selected time interval. The dashed blue line refers to the fit of the low-frequency part of the spectrum.

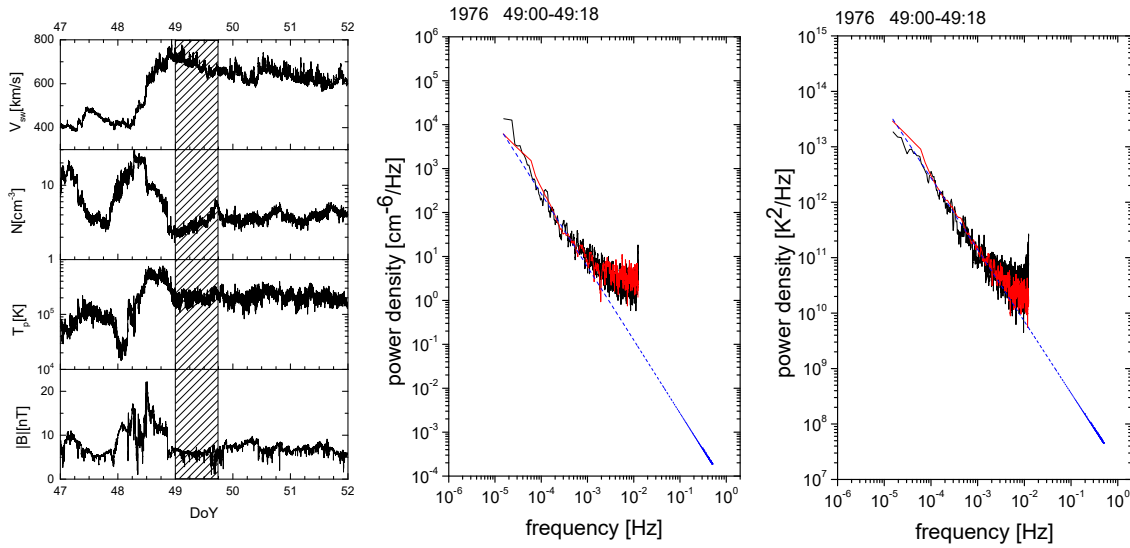


**Fig. 2.** Same as Fig. 1, but at 0.9 AU.

the simulation. Kasper et al. (2002) showed that

$$T_R = T_{\parallel}(\hat{R} \cdot \hat{b})^2 + T_{\perp}[1 - (\hat{R} \cdot \hat{b})^2], \quad (2)$$

where  $T_R$  corresponds to  $T_p$  in Helios measurements,  $\hat{R} \cdot \hat{b} = \cos(\theta_{BR})$ , with  $\hat{R}$  the unit vector corresponding to the radial direction, and  $\hat{b}$  the unit vector corresponding to the magnetic field direction. Assuming a given anisotropy  $T_{\perp}/T_{\parallel}$  (e.g., 1.4 as derived in Marsch et al. 1982, at 0.29 AU) and computing  $\cos(\theta_{BR})$  from magnetic field measurements, we are able to provide  $T_{\parallel}$  and  $T_{\perp}$  by inverting Eq. (2).

### 2.1. Instrumental noise

The original power spectral density of the proton number density is shown in the middle panel of Fig. 1 by the black curve. The dashed blue line represents the power law fit to the

low-frequency range, and the red curve is the synthetic spectrum obtained by simulation. The two spectra are remarkably similar, in particular, the spectral flattening starts at approximately the same frequency of  $2 \times 10^{-4}$  Hz, although none of the parameters used in the simulation, that is, the number density  $N$ , the proton temperature  $T_p$ , and the magnetic field  $B$ , has any spectral break around this frequency. Comparable results, although at a lower degree of similarity, are shown in the right panel for  $T_p$  in the same format. In this case, we used Eq. (2) to compute the temperature radial component corresponding to simulated data. We repeated the same analysis on the fast stream detected at 0.9 AU, spanning the time interval from day 49:00:00 to day 49:18:12, as shown in the left panel of Fig. 2. In this case, the anisotropy was set to 0.85, as derived in Marsch et al. (1982). The power spectra show that the amplitude of the fluctuations is reduced and the flattening is less pronounced than at 0.3 AU. We are able to reproduce the behavior of the power

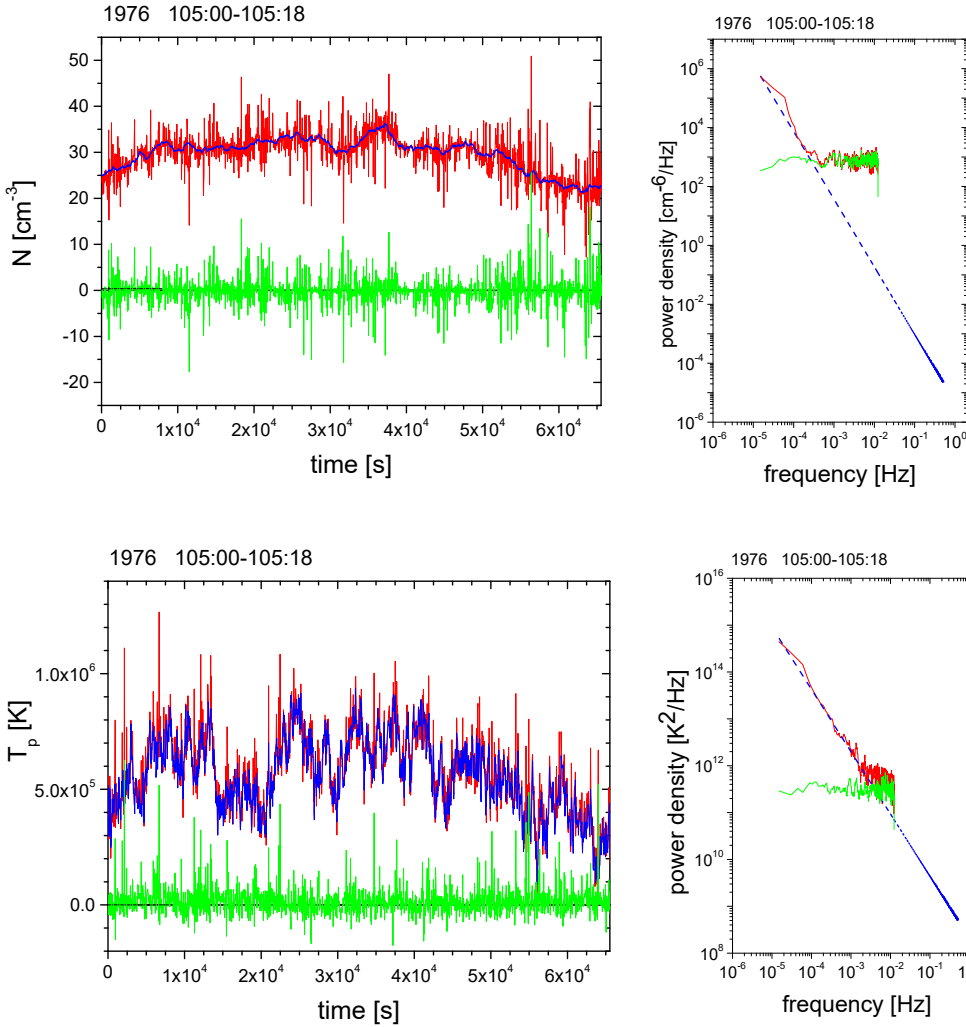


**Fig. 3.** *Left panel:* time series of number density of data derived from inverse transform of the fit of the low-frequency part of the spectrum (blue trace) used as input data for simulated measurement (red trace) and difference between the previous signals (green trace). *Right panel:* power spectral density of the number density with the same color code as in left panel.

**Fig. 4.** Same as Fig 3, but for the radial temperature.

spectra of number density and temperature to a good degree here as well.

To clarify the artificial effect introduced by the plasma sensor on the estimate of the proton number density, we study Fig. 3. The blue trace in the left-hand panel of this figure shows 40.5 s averages of the 1 s time series of the proton number density we used as input parameter for our simulation. The red trace instead shows values of the same parameter as measured by the simulated sensor. The spiky appearance of the latter suggests that the sampling procedure operated by the sensor introduces some noise, which is highlighted by the green trace, which shows the difference between the two previous time series. The right-hand panel shows power density spectra of the previous signals identified by the same color code. The noise spectrum is rather flat, typical of white noise, and its power density level determines the location of the spectral break around  $2 \div 3 \times 10^{-4}$  Hz, as shown by the red trace. Similarly to what happens for the number density spectrum, the spectral noise introduced by the proton temperature measurement determines the frequency location of the spectral break in the temperature spectrum, as shown in Fig. 4. In this case, the level of the spectral noise has a weaker effect on the temperature spectrum. This causes a weaker flattening at high frequencies and a shift of the spectral break to higher frequencies by about one decade. Our conjecture is that the error level in the measurement is related to the relative amplitude of the velocity fluctuations induced on the particle velocity distribution by the Alfvénic fluctuations, hence we would expect this

phenomenon to be less relevant with increasing heliocentric distance. The high-speed stream observed at 0.9 AU (Fig. 2) shows a much weaker flattening for both number density and temperature. As a cross check of the effectiveness of the mechanism described above, we performed on this stream the same analysis, whose results are shown in Figs. 5 and 6 for number density and temperature, respectively. These graphs confirm the role of spectral noise in determining the level of high-frequency flattening and the location of the frequency break.

In Fig. 7, we finally show the result produced by this simulation with regard to the proton number density (left panel) and temperature (right panel) intermittency studied in terms of the kurtosis values. Results from the intermittency analysis highlight the Gaussian character of the 1 s values that were used as input and the rather intermittent character of the 40.5 s values obtained from our simulation, which is quite similar to the intermittency that is observed in real data. These results also agree with a radial evolution of the number density intermittency (Bruno et al. 2014) and show for the first time, to our knowledge, a similar radial trend for the proton temperature.

Although the results are quite encouraging, one aspect of this simulation requires a moment of reflection. The synthetic density and temperature 1 s data that we used to feed the code to produce 40.5 s density and temperature moments, are characterized by fluctuations with typical Gaussian statistics, by construction. However, the fluctuations of the time series of the resulting 40.5 s measurements are clearly intermittent, just like real data.

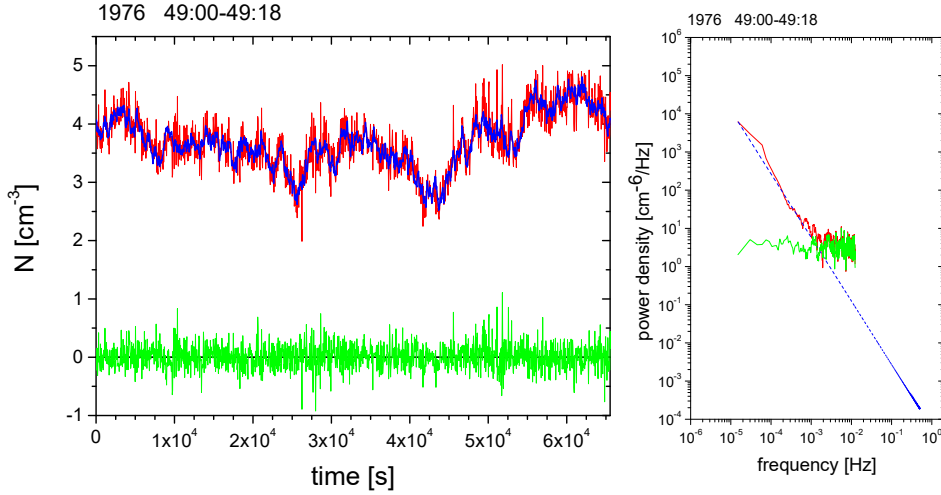


**Fig. 5.** Results of the analysis for the number density, shown in the same format as in Fig. 2, but for the wind stream observed at 0.9 AU.

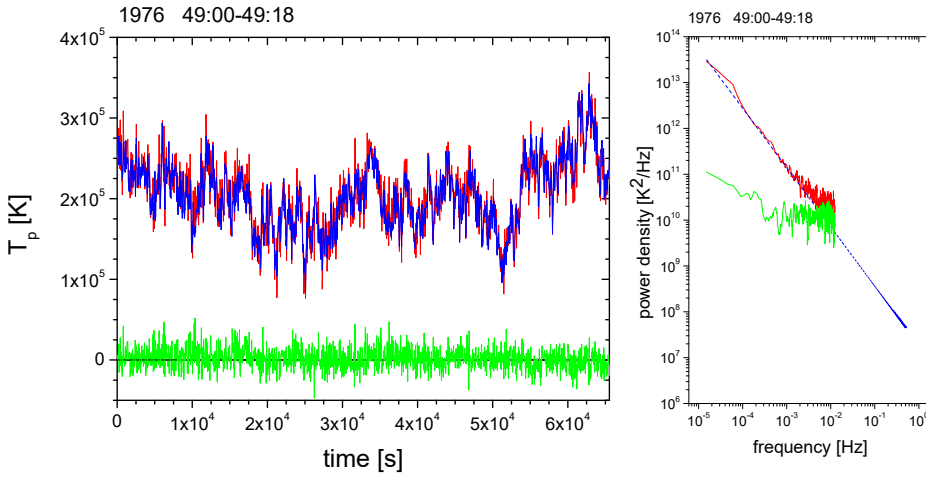


**Fig. 6.** Results of the analysis for the temperature, shown in the same format as in Fig. 4, but for the wind stream observed at 0.9 AU.

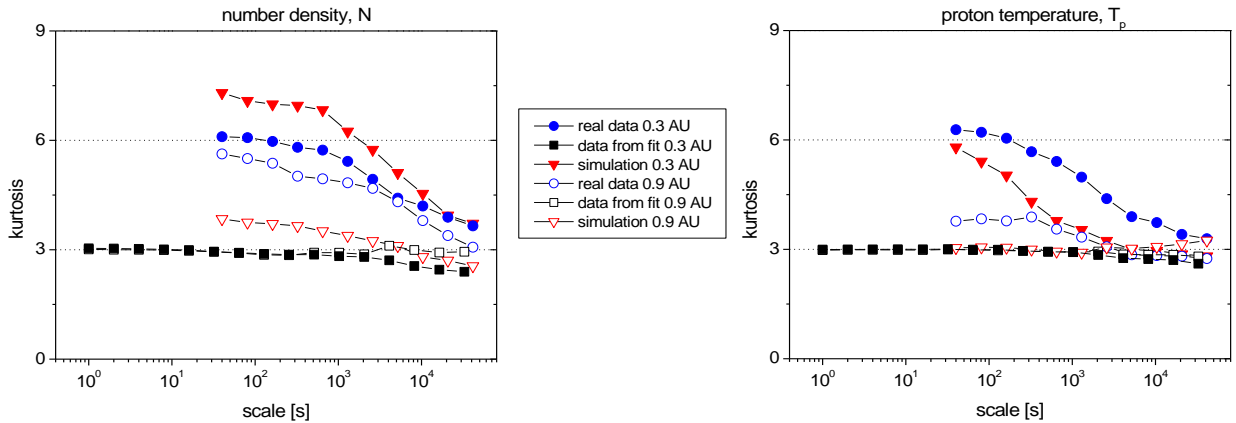


**Fig. 7.** Kurtosis values vs. timescales of the number density (*left panel*) and radial temperature (*right panel*) for real data (blue circles), simulation (red triangles), and 1 s data (black squares) used as input for the simulations at 0.3 AU (full symbols) and 0.9 AU (empty symbols). The same color code and symbols are adopted in both panels.

This result is only apparently contradictory when we consider that most of the noise that is generated during the VDF sampling is due to the arc-like motion of the VDF within the 3D velocity space. This motion is due to Alfvénic fluctuations constructed on real magnetic field observations, which, as we know from the literature (see the review by Bruno & Carbone 2013 and the many references listed in there), are increasingly intermittent

from large to increasingly smaller scales. This clearly introduces a first element of non-Gaussianity to which we have to add the complexity of the moments calculation, which is not a simple snapshot picture. As a consequence, we should not expect a linear response from the moments computation, and the intermittent character of the 40.5 s density and temperature time series should be less surprising. When the amplitude of the Alfvénic

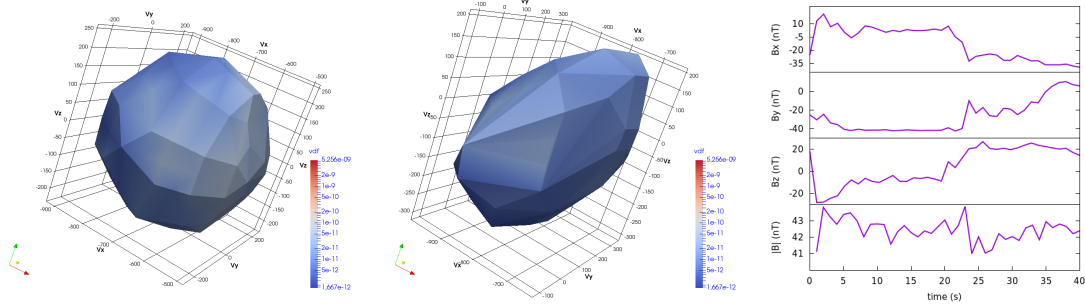


**Fig. 8.** *Left panel:* isotropic 3D VDF in phase space used as input for the simulations. *Middle panel:* anisotropic 3D VDF in phase space obtained as output from simulations. *Right panel:* time series of the magnetic field components and magnitude used in the simulation.

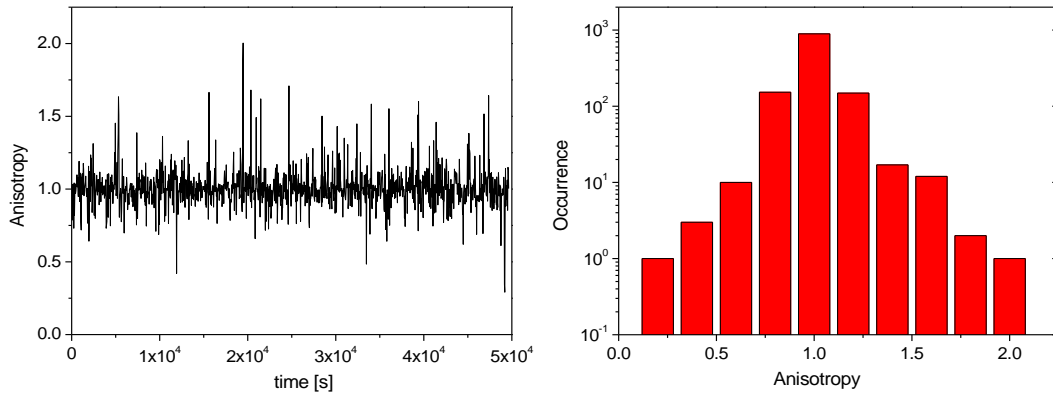


**Fig. 9.** Time series of the measured anisotropy (*left*) and histogram of relative values (*right*).

fluctuations decreases with distance, we observe less intermittency, as expected. When we completely remove the Alfvénic fluctuations from our simulation, we obtain time series of the number density and temperature with the same statistical character as the input data.

## 2.2. Effects on the temperature

Another interesting effect that can be analyzed in our model is the influence on the measured temperature of a sampling time on the same order, or greater, than the wave period. To this end, we show the result of a simulation in which the bulk velocity components change as described in Sect. 2, but now we considered fixed density and temperature as input, which we set to  $N = 30 \text{ cm}^{-3}$  and  $T_{\parallel} = T_{\perp} = 5.8 \times 10^5 \text{ K}$ . This choice was made to highlight the specific effect of the moving VDF in phase space while removing the influence of a continuous change in the input density and temperature values. In this simulation we used the same original magnetic field at 1 s resolution as in the fast wind stream at 0.3 AU. As an example, we show in the left panel of Fig. 8 the input VDF, and in the middle panel the VDF as measured when the bulk velocity changes according to the magnetic field reported in the right panel. Although the VDF to be sampled is isotropic in all the subintervals that make up the sampling time, the measured VDF is clearly somewhat anisotropic. In particular, we find that parallel and perpendicular temperatures considered separately are, in the majority of cases, higher than those that are input, as discussed in [Verscharen & Marsch \(2011\)](#) and [Perrone et al. \(2014\)](#). However, there is no evidence of a steady prevalence of one component over the other one. In Fig. 9 we report the time series of the measured anisotropy together with the occurrence of the different values. The “real” temperature

anisotropy, which is equal to 1, is still the most probable measure, under our conditions. Nevertheless, the anisotropy in a relevant number of the measured VDFs is either greater or smaller than the one in input. This result corroborates the interpretation of Helios observations, within fast Alfvénic wind at short heliocentric distances, that  $T_{\perp}/T_{\parallel} > 1$  is mainly due to a real physical mechanism ([Marsch et al. 1982](#)) and not to a systematic erroneous response of the sensor caused by the sloshing motion of the VDF within the velocity space.

As described above, fluctuations of the background magnetic field vector, and as a consequence, of the bulk velocity vector  $V$  due to Alfvénic fluctuations, cause the observed variability in our simulation. Thus, we expect that a higher variability in  $V$  would produce a higher variability in the anisotropy. This is exactly what is shown in the left panel of Fig. 10, where anisotropy values are plotted versus  $\sigma(V)$ , the standard deviation of the velocity fluctuations recorded during the sampling of each VDF. For low values of  $\sigma(V)$ , the anisotropy is near one, but becomes increasingly more scattered for increasing values of  $\sigma(V)$ . The extreme cases of deformation are found where the magnetic field has some abrupt change during the measure, such as sudden jumps, spikes, or switchbacks. The VDF reported in Fig. 8 refers to one of these special cases. The reason for a resulting modified anisotropy is that, during the measure, the tip of the actual bulk velocity vector performs an unpredictable pattern on a sphere. This sphere has a constant radius approximately equal to the Alfvén velocity  $V_A$  and is centered on the phase speed of the Alfvénic fluctuations moving away from the Sun, that is, roughly  $V + V_A$  ([Matteini et al. 2015](#)). In this motion, small oscillations are interspersed with sudden jumps. As a result, some bins within the velocity space might record a larger or smaller number of particles compared to the situation in which the

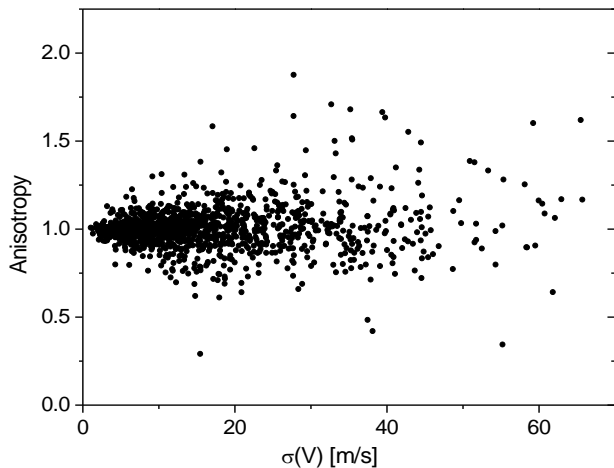


**Fig. 10.** Scatter plot of the anisotropy as a function of the standard deviation of the velocity fluctuations during the measurement.

sampling time is sufficiently fast for the effect of fluctuations on the distribution to be neglected. The reason is that in one case, the bulk velocity moves according to the stepping direction of the energy interval, while in the other case, the VDF moves beyond the particular energy-angle that is sampled at a given moment. As a consequence, the measured distribution function may appear quite irregular, but this is just an artifact (which is added to the true physical effects) produced by the sampling process, during which the distribution moves in order to remain aligned with the fluctuating magnetic field. A similar conclusion has been pointed out first by [Maruca & Kasper \(2013\)](#).

### 3. Discussion

We performed a numerical test to better understand the origin of the enhanced spectral flattening for proton number density and proton temperature spectra observed in Helios data during the perihelion passage, when the s/c was immersed in fast and Alfvénic solar wind. This spectral feature has been interpreted as the spectral signature of sound-like perturbations generated locally by the parametric decay of large-amplitude Alfvénic fluctuations ([Marsch & Tu 1990](#)). However, it has recently been shown ([Verscharen & Marsch 2011](#); [Perrone et al. 2014](#); [Nicolaou et al. 2019](#)) that large-amplitude Alfvénic fluctuations are able to move around the particle velocity distribution in phase space, and this phenomenon might be important for an electrostatic analyzer whose sampling time is comparable with the period of these fluctuations. Thus, in order to test the relevance of these oscillations for the final determination of the moments of the distribution, we mimicked the sampling process of the proton velocity distribution performed by an electrostatic analyzer, similar to the one on board the Helios mission ([Schwenn et al. 1975](#)), in the presence of Alfvénic fluctuations. Synthetic input parameters at 1 s that are required to build the particle distribution, such as the proton number density and temperature, were inferred from a particular spectral analysis, as described in the previous section, while magnetic field data were derived from real measurements at 4 Hz resampled at 1 Hz, corresponding to the sampling time for each energy channel. In addition, these values of a 1 s magnetic field and number density were used to build the necessary Alfvénic fluctuations at frequencies comparable with the sampling time of the analyzer. We showed that the motion of the VDF has an unpredictable

influence on the moments computations as a result of the Alfvénic fluctuations, producing noisy measurements. Although the idea underlying our numerical test is simple and does not take other perturbations into account, such as compressive magnetosonic fluctuations or advected discontinuities, the results are remarkable. We were able to reproduce – to a rather satisfactory degree – the flattening observed in density and temperature spectra. This flattening might be the result of a combination of distinct effects, but we showed that instrumental effects cannot be ignored when the sensor sampling time is comparable to the period of large-amplitude Alfvénic fluctuations. Furthermore, we showed that a relatively long sampling time may produce a deviation from the real anisotropy because the VDF may have a large arc-like motion in the field of view of the instrument. These results are relevant for future studies concerning the design of new plasma sensors. A faster acquisition time of the whole distribution would provide less noisy results. In this respect, we can predict that number density and proton temperature spectra based on observations provided by the Solar Wind Analyser (SWA) on board Solar Orbiter will show a much reduced effect because the sampling frequency (1 Hz) of this instrument is higher than that of Helios.

*Acknowledgements.* This work was partially supported by the Italian Space Agency (ASI) under contract ACCORDO ATTUATIVO n. 2018-30-HH.O. Results from the data analysis presented in this paper are directly available from the authors upon request. We warmly thank the anonymous Referee for her/his valuable suggestions and comments.

### References

- Balogh, A. 2005, *Payload and Mission Definition in Space Sciences* (Cambridge, UK: Cambridge University Press), 243
- Bavassano, B., Dobrowolny, M., Mariani, F., et al. 1982, *J. Geophys. Res.*, **87**, 3617
- Bavassano, B., Pietropaolo, E., & Bruno, R. 2000, *J. Geophys. Res.*, **105**, 12697
- Bruno, R., & Carbone, V. 2013, *Liv. Rev. Sol. Phys.*, **10**, 2
- Bruno, R., Carbone, V., Primavera, L., et al. 2004, *Ann. Geophys.*, **22**, 375
- Bruno, R., Telloni, D., Primavera, L., et al. 2014, *ApJ*, **786**, 53
- Coleman, P. J. 1968, *ApJ*, **153**, 371
- D’Amicis, R., De Marco, R., Bruno, R., & Perrone, D. 2019, *A&A*, **632**, A92
- Derby, N. F., Jr. 1978, *ApJ*, **224**, 1013
- Frisch, U. 1995, *Turbulence: The Legacy of A. N. Kolmogorov* (Cambridge, UK: Cambridge University Press), 296
- Goldstein, M. L. 1978, *ApJ*, **219**, 700
- Kasper, J. C., Lazarus, A. J., & Gary, S. P. 2002, *Geophys. Res. Lett.*, **29**, 1839
- Kolmogorov, A. N. 1941, *Dokl. Akad. Nauk. SSSR*, **30**, 301
- Malara, F., Primavera, L., & Veltri, P. 2000, *Phys. Plasma*, **7**, 2866
- Malara, F., Primavera, L., & Veltri, P. 2001, *NPGEO*, **8**, 159
- Marsch, E., & Tu, C.-Y. 1990, *J. Geophys. Res.*, **95**, 11945
- Marsch, E., Mühlhäuser, K.-H., Schwenn, R., et al. 1982, *J. Geophys. Res.*, **87**, 52
- Maruca, B. A., & Kasper, J. C. 2013, *Adv. Space Res.*, **52**, 723
- Matteini, L., Horbury, T. S., Pantellini, F., Velli, M., & Schwartz, S. J. 2015, *ApJ*, **802**, 11
- Musmann, G., Neubauer, F. M., & Lammers, E. 1977, *J. Geophys. Z. Geophys.*, **2**, 591
- Nicolaou, G., Verscharen, D., Wicks, R. T., & Owen, J. 2019, *ApJ*, **886**, 101
- Perrone, D., Bourouaine, S., Valentini, F., Marsch, E., & Veltri, P. 2014, *J. Geophys. Res. Space Phys.*, **119**, 2400
- Primavera, L., Malara, F., & Veltri, P. 1999, *ESA SP*, **448**, 1999
- Primavera, L., Malara, F., & Veltri, P. 2003, *AIP Conf. Proc.*, **679**, 505
- Sakai, J. I., & Sonnerup, B. U. O. 1983, *J. Geophys. Res.*, **88**, 9069
- Schwenn, R., Rosenbauer, H., & Miggenrieder, H. 1975, *Raumfahrtforschung*, **19**, 226
- Stansby, D., Salem, C., Matteini, L., & Horbury, T. 2018, *Sol. Phys.*, **293**, 155
- Terasawa, T., Hoshino, M., Sakai, J.-I., & Hada, T. 1986, *J. Geophys. Res.*, **91**, 4171
- Tu, C.-Y., & Marsch, E. 1995, *Space Sci. Rev.*, **73**, 1
- Tu, C.-Y., Marsch, E., & Thieme, K. M. 1989, *J. Geophys. Res.*, **94**, 11739
- Tu, C.-Y., Marsch, E., & Rosenbauer, H. 1991, *Ann. Geophys.*, **9**, 748
- Verscharen, D., & Marsch, E. 2011, *Ann. Geophys.*, **29**, 909